物 理 化 学 学 报

Acta Phys. -Chim. Sin. **2023,** *39* (2), 2203048 (1 of 10)

[Article] doi: 10.3866/PKU.WHXB202203048 www.whxb.pku.edu.cn

Two-Step Sequential Blade-Coating Large-Area FA-Based Perovskite Thin Film *via* a Controlled PbI_2 Microstructure

Yongtao Wen [1,2], Jing Li [1], Xiaofeng Gao [3], Congcong Tian [1], Hao Zhu [3], Guomu Yu [1], Xiaoli Zhang [4], Hyesung Park [5,*], Fuzhi Huang [1,2,*]

[1] State Key Laboratory of Advanced Technology for Materials Synthesis and Processing, Wuhan University of Technology, Wuhan 430070, China.

[2] Foshan Xianhu Laboratory of the Advanced Energy Science and Technology Guangdong Laboratory, Foshan 528216, Guangdong Province, China.

[3] International School of Materials Science and Engineering, Wuhan University of Technology, Wuhan 430070, China.

[4] School of Materials Science and Engineering, Zhengzhou University, Zhengzhou 450001, China.

[5] Department of Materials Science and Engineering, Graduate School of Semiconductor Materials and Devices Engineering, Perovtronics Research Center, Low Dimensional Carbon Materials Center, Ulsan National Institute of Science and Technology, Ulsan 44919, Republic of Korea.

Abstract: Solar cells, which are excellent alternatives to traditional fossil fuels, can efficiently convert sunlight into electricity. The intensive development of high-performance photovoltaic materials plays an important role in environmental protection and the utilization of renewable energy. Organic–inorganic hybrid perovskite materials, with a formula of ABX_3 (A = methylammonium (MA) or formamidinium (FA); B = Pb or Sn; X = Cl, I, or Br), have exhibited remarkable commercial prospects in high-performance photovoltaic devices owing to their long carrier diffusion length, excellent light absorption properties, high charge carrier mobility, and weak exciton binding energy. Recently, perovskite solar cells, fabricated using halide perovskite materials as light-absorbing layers, have achieved remarkable results; their certified power conversion efficiency has continuously improved and reached 25.7%. However, high-performance devices are usually fabricated using spin-coating methods with active areas below 0.1 cm^2. Hence, long-term research goals include achieving a large-scale uniform preparation of high-quality photoactive layers. The current one-step preparation of perovskite films involves the nucleation-crystalline growth process of perovskite. Auxiliary processes, such as using an anti-solvent, are often required to increase the nucleation rate and density of the film, which is not suitable for industrial large-area preparation. Additionally, the large-area preparation of perovskite films by spin-coating will result in different film thicknesses in the center and edge regions of the film due to an uneven centrifugal force. This will cause intense carrier recombination in the thicker area of the film and weak light absorption in the thinner area, which will reduce the performance of the device. To address these problems, the development of a large-area fabrication method for high-performance perovskite light-absorbing layers is essential. In this study, a two-step sequential blade-coating strategy was developed to prepare the FA-based perovskite layer. In general, PbI_2 easily forms a dense film; therefore, formamidinium iodide (FAI) cannot deeply penetrate to completely react with PbI_2. The PbI_2 residue is therefore detrimental to charge transportation. To fabricate the desired porous PbI_2 film, tetrahydrothiophene 1-oxide (THTO) was introduced into the PbI_2 precursor solution. By forming PbI_2·THTO complexes, PbI_2 crystallization is controlled, resulting in the formation of vertically packed PbI_2 flaky crystals. These crystals provide nanochannels for easy FAI penetration. The 5 cm × 5 cm modules fabricated through this strategy achieved a high

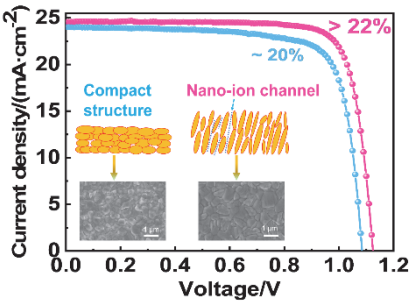

Received: March 28, 2022; Revised: April 22, 2022; Accepted: April 25, 2022; Published online: April 29, 2022.

*Corresponding authors. Emails: hspark@unist.ac.kr (H.P.); fuzhi.huang@whut.edu.cn (F.H.).

The project was supported by the National Key Research and Development Plan (2019YFE0107200, 2017YFE0131900), the National Natural Science Foundation of China (21875178, 52172230, 91963209), the Fundamental Research Funds for the Central Universities (WUT: 202443004), and Foshan Xianhu Laboratory of the Advanced Energy Science and Technology Guangdong Laboratory (XDT2020-001, XHT2020-005).

科技部重点研发计划(2019YFE0107200, 2017YFE0131900), 国家自然科学基金(21875178, 52172230, 91963209), 中央高校基本科研业务费专项资金(WUT: 202443004), 先进能源科学与技术广东省实验室佛山分中心佛山仙湖实验室开放基金(XDT2020-001, XHT2020-005)资助项目

efficiency of 18.65% with excellent stability. This indicates that the two-step sequential blade-coating strategy has considerable potential for scaling up the production of perovskite solar cells.

Key Words: Perovskite solar cell; Two-step; Blade-coating; Printing; Module

控制碘化铅形貌两步连续刮涂法大面积制备甲脒基钙钛矿薄膜

文永涛[1,2]，李静[1]，高晓峰[3]，田聪聪[1]，朱昊[3]，余国木[1]，张晓俐[4]，Hyesung Park [5,*]，黄福志[1,2,*]

[1]武汉理工大学材料复合新技术国家重点实验室，武汉 430070

[2]先进能源科学与技术广东省实验室佛山分中心佛山仙湖实验室，广东 佛山 528216

[3]武汉理工大学材料科学与工程国际化示范学院，武汉 430070

[4]郑州大学材料科学与工程学院，郑州 450001

[5] Department of Materials Science and Engineering, Graduate School of Semiconductor Materials and Devices Engineering, Perovtronics Research Center, Low Dimensional Carbon Materials Center, Ulsan National Institute of Science and Technology, Ulsan 44919, Republic of Korea

摘要：钙钛矿太阳能电池在实现高性能光伏器件方面展现出巨大的商业化应用前景，但面临着一个最主要的挑战是开发工业化规模生产的大面积高质量钙钛矿薄膜制备工艺。在本研究中，为解决大面积印刷难题，通过两步连续刮涂法制备甲脒基钙钛矿吸光层。两步法中第一步沉积的PbI_2很容易形成致密的薄膜，这将导致后续沉积的有机胺盐无法和PbI_2充分完全反应，在钙钛矿薄膜中残留PbI_2，这会严重影响载流子的传输。为了实现理想的多孔PbI_2薄膜结构，我们通过在PbI_2前驱体溶液中引入四亚甲基亚砜(THTO)。通过形成PbI_2·THTO络合物，PbI_2的结晶过程被有效控制，易形成片状的PbI_2晶粒并沿着垂直基底方向上排列，得到了理想的纳米通道。这为后续的有机胺盐渗入提供了理想的纳米通道。最终5 cm × 5 cm模组实现了18.65%的功率转化效率，并具有出色的存储和热稳定性。这一结果展现了两步连续刮涂法策略在制备大面积钙钛矿太阳能电池方面具备一定的优势。

关键词：钙钛矿太阳能电池；两步法；刮涂；印刷；模组

中图分类号：O646

1 Introduction

Perovskite solar cells (PSCs) have attracted much attention due to their high power conversion efficiency (PCE), printability, and low-cost preparation [1–7]. The certified PCE of PSCs has exceeded 25% [8], which shows a huge prospect for future commercial applications [9]. However, the reported high-performance devices were all prepared through spin-coating methods, normally using anti-solvent strategies to prepare high-quality perovskite films [10–12]. In fact, the photoelectric performance of large-area PSCs prepared by a combination of spin-coating and anti-solvent will be greatly reduced [13,14]. Therefore, a process that is compatible with large-area high-quality perovskite films is currently in urgent need to accelerate the process of industrialization [15].

Blade-coating method is a process with simple operation and efficient material utilization, and has been widely regarded as an effective method for preparing large-area thin films [16–24]. For a blade-coating process, the substrate is firstly placed on a platform, and then the precursor solution is coated on the substrate by moving the blade to form a wet film. After the solvent evaporates, the solute crystallizes on the substrate to form a thin film. The quality of the perovskite film can be improved by changing the precursor solution composition or through solvent engineering [25,26]. Therefore, a large amount of research has focused on one-step coating of MA-based perovskites that are quite easy to control their crystallization [27,28], but there are few studies on FA-based perovskites that are more stable and efficient [29–33]. The main reason is that the nucleation and growth process of FA-based perovskites are difficult to control through the one-step blade-coating process [34].

In contrast, the two-step sequential blade-coating deposition method is much easier to handle, as it does not involve the nucleation process of the perovskite. The two-step method first deposits the PbI_2 film on the substrate, and then second coating of (FAI) undergoes continuous solid-phase reaction with PbI_2 to

transform into a perovskite film [35,36]. The interaction process between PbI_2 and FAI molecules effectively solves the uncontrollable nucleation issue of FA-based perovskites in the one-step process. Therefore, the two-step deposition is considered to be a more controllable and reliable method for uniformly preparing thin films on a large area. One of the main problems in the two-step process is that the compact PbI_2 film is not conducive to the complete conversion of perovskite as the FAI molecules are hard to diffuse to the bottom of the film. Therefore, a lot of research is devoted to controlling the morphology of PbI_2 to form a porous structure, providing nanochannels for FAI diffusion, and also increasing the specific surface area between PbI_2 and FAI molecules to facilitate the reaction. For example, Li *et al.* [37] adopted multistep annealing method to deposit a porous PbI_2 film and improved the quality and uniformity of perovskite films. Choy *et al.* [38] used the PbI_2 precursor solution to incorporate a small amount of reasonably selected additives to form a self-assembled porous PbI_2, which significantly promoted the conversion of perovskite without any PbI_2 residues. Huang *et al.* [39] reported a vertically aligned PbI_2 film grown from an ionic liquid. The vertically grown structure has numerous nanoscale ion channels, which facilitates the rapid and stable conversion to $FAPbI_3$, and finally achieves 24.1% PCE and excellent thermal stability. For the two-step process, it has been strongly proved that controlling the morphology and structure of PbI_2 is essential for the preparation of high-quality perovskite films. However, high-performance devices are all based on spin-coating, and there are relatively few research reports on the scalable process, such as blade-coating. We prepared the perovskite film by a two-step blade-coating method and found that the deposited PbI_2 film with layered crystals is not conducive to the second step of the reaction. Therefore, how to realize the PbI_2 film with regular and continuous nanochannels is extremely essential for the sequential blade-coating method. In this work, THTO is introduced into the PbI_2 *N*,*N*-dimethylformamide (DMF) solution to control the crystallization of PbI_2, which results in a continuous porous layer composed of vertical packed flaky PbI_2 nanocrystals. This strategy facilitates the diffusion of organic amine salts and addresses the issue of incomplete reaction between PbI_2 and organic amine salts in the two-step method. In addition, high-quality perovskite films were prepared by combining the blade coating method to solve large-area printing.

2 Experimental

2.1 Materials

$SnCl_2{\cdot}2H_2O$ was purchased from Aladdin, and urea was purchased from Alfa Aesar. DMF, isopropyl alcohol (IPA), and dimethyl sulfoxide (DMSO) were purchased from Sigma-Aldrich. Lead iodide (PbI_2), FAI and methylammonium chloride (MACl) were purchased from Xi'an Polymer Light Technology Corp. THTO was purchased from Acros. Spiro-OMeTAD was purchased from Shenzhen Feiming Science and Technology Co., Ltd.

2.2 Precursor preparation

The PbI_2 solution was prepared by dissolving 600 mg PbI_2 powder in mixed solvents (DMF: additives). For the preparation of the solution of organic amine salts, 60 mg FAI and 15 mg MACl were dissolved in 1 mL IPA.

2.3 Device fabrication

F-doped SnO_2 glass substrates (FTO) were etched by femtosecond laser, and followed by ultrasonic cleaning through detergent, deionized water and ethanol for 20 min, respectively. The substrates were treated by ultraviolet (UV) light for 15 min before deposition of SnO_2. The SnO_2 film was prepared by chemical bath deposition (CBD) according to our previous report. The perovskite films were deposited on the SnO_2 substrate *via* the two-step sequential blade-coating method in ambient environment. First, 60 μL of PbI_2 precursor solution (5 cm × 5 cm substrate) was dropped on the substrate to form a horizontal line, and then the coater with the blade height of 0.48 mm above substrate was controlled to move at a speed of 4 $mm{\cdot}s^{-1}$. The wet films were dried immediately by air blowing and then annealed at 70 °C for 1 min to dry films. After the substrate cooled down to room temperature, the mixture solution of FAI: MACl (60 mg: 15 mg in 1 mL IPA) was bladed onto the PbI_2 films (generally 80 μL for 5 cm × 5 cm substrate), then annealed at 150 °C for 15 min for perovskite crystallization. After cooling down, a 5 $mg{\cdot}mL^{-1}$ t-BAI/IPA solution was spun onto the small size blade-coated perovskite films and followed by annealing at 100 °C for 10 min. The Spiro-OMeTAD solution was prepared by dissolving 91.4 mg Spiro-OMeTAD, 35.65 μL 4-tert-butylpyridine, 21 μL Li-TFSI (from 520 $mg{\cdot}mL^{-1}$ stock acetonitrile solution) and 11 μL FK209 (300 $mg{\cdot}mL^{-1}$ stock acetonitrile solution) in 1 mL chlorobenzene (CBZ). After stirring adequately, the desired solution was spun onto perovskite films by 4000 $r{\cdot}min^{-1}$ for 20 s. Finally, about 80 nm Au was deposited by thermal evaporation method.

2.4 Characterizations

The field emission scanning electron microscope (FESEM, Zeiss Ultra Plus) and atomic force microscope (AFM, SPM9700, Shimadzu, Japan) were used to characterize the surface morphology and microstructure of all PbI_2 films, perovskite films, and device structures. The crystal phase of PbI_2 and perovskite films was characterized by an X-ray diffractometer (XRD, D8 Advance). The Fourier transform infrared (FTIR) spectra were obtained using Nexus. The steady-state photoluminescence (PL) spectra were characterized by a PL microscopic spectrometer (Flex One, Zolix, China). The *J*–*V* curves of all PSCs were measured in room environment using a Keithley 2400 source meter and an AM 1.5 G solar simulator (Oriel 94023 A, 300 W). A standard silicon cell (Oriel, VLSI standards) was used to calibrate the intensity of light to 100 $mW{\cdot}cm^{-2}$. The test scan rates for 0.16 cm^2 devices and 5 cm × 5 cm modules with an aperture area of 10 cm^2 were 10 and 50 $mV{\cdot}s^{-1}$, respectively. The external quantum efficiency (EQE)

was tested using commercial EQE system (Newport).

3 Results and discussion

For the two-step blade-coating process, the most important step is the deposition of PbI_2 layer. Fig. 1 shows the fabrication process of perovskite films *via* the blade-coating method from compact-PbI_2 (labeled C-PbI_2) and THTO additive-induced vertical nanochannel-PbI_2 (labeled NC-PbI_2) films. Traditionally, PbI_2 films are often obtained by volatilizing the solvent through thermal annealing [40], but the pores structure are often discontinuous. The main reason is that the PbI_2 grains are small, and in a certain range, it is still compact PbI_2, which affects the permeation of FAI molecules. Thus, the compact PbI_2 crystals, especially distant from the contact interface, cannot be fully converted into perovskites. While by introducing THTO into the PbI_2 precursor solution, PbI_2 will coordinate with THTO molecule which is a sulfur-donor ligand to form coordination complexes PbI_2-THTO after volatilization of DMF at 70 °C. THTO acts as a Lewis base additive to alter the crystallization of PbI_2, thus inducing flaky PbI_2 crystals. The vertical stack of the large flaky PbI_2 grains leads to continuous nanochannel in the films. This structure subsequently offered a widely enlarged contact area to facilitate interfacial reaction with FAI/MACl and greatly improved perovskite crystallization.

Fig. 2a,b shows the scanning electron microscope (SEM) images of the surface and cross-section of the C-PbI_2 film, where it can be observed that the film is composed of layered, and dense small crystals. In contrast, the NC-PbI_2 (Fig. 2d,e) films have flaky large grains of PbI_2 and continuous regular nanochannels. After addition of THTO, the thickness of the NC-PbI_2 film increases from ~370 nm (Fig. 2b) of C-PbI_2 film to ~595 nm (Fig. 2e) due to loose stacking of flaky PbI_2 that also alters the surface roughness. Fig. S1a,b (Supporting Information) show atomic force microscopy (AFM) images of the C-PbI_2 and NC-PbI_2 films, respectively. The roughness (R_q) of the films increases from 16.6 nm for C-PbI_2 to 28.0 nm for NC-PbI_2. After the second blade-coating step of the organic mixed salts of FAI/MACl, the PbI_2 film is converted to perovskites. From the cross-sectional SEM images of the perovskite films (Fig. 2c,f), it can be observed that the perovskite film converted by C-PbI_2 consists of several small grains in the normal direction and has a large amount of PbI_2 residual at the interface, while the perovskite film converted by NC-PbI_2 has a single large grain in the normal direction and no residual PbI_2. The single-grain structure can reduce the number of grain boundaries in the film, facilitate carrier transport and increase carrier lifetime, thereby improve photoelectric conversion performance. The vertical stacked flaky PbI_2 in the NC-PbI_2 film not only offers continuous nanochannel for FAI/MACl diffusion, but also has a greatly enlarged surface area available for the subsequent reaction, thus forming a complete reacted large grain perovskite.

To reveal the mechanism for the generation of vertical nanochannels in NC-PbI_2 thin films, the pure PbI_2·THTO solution was used for blade-coating. The corresponding X-ray diffraction (XRD) results of the obtained film (Fig. S2) show that a strong PbI_2·THTO complex peak appeared at 7.8°. The complex crystals are aligned vertically in the film direction as shown in the cross-sectional SEM images (Fig. 2i). In addition, Fig. 2j shows the XRD results of PbI_2 (DMF/DMSO) and PbI_2

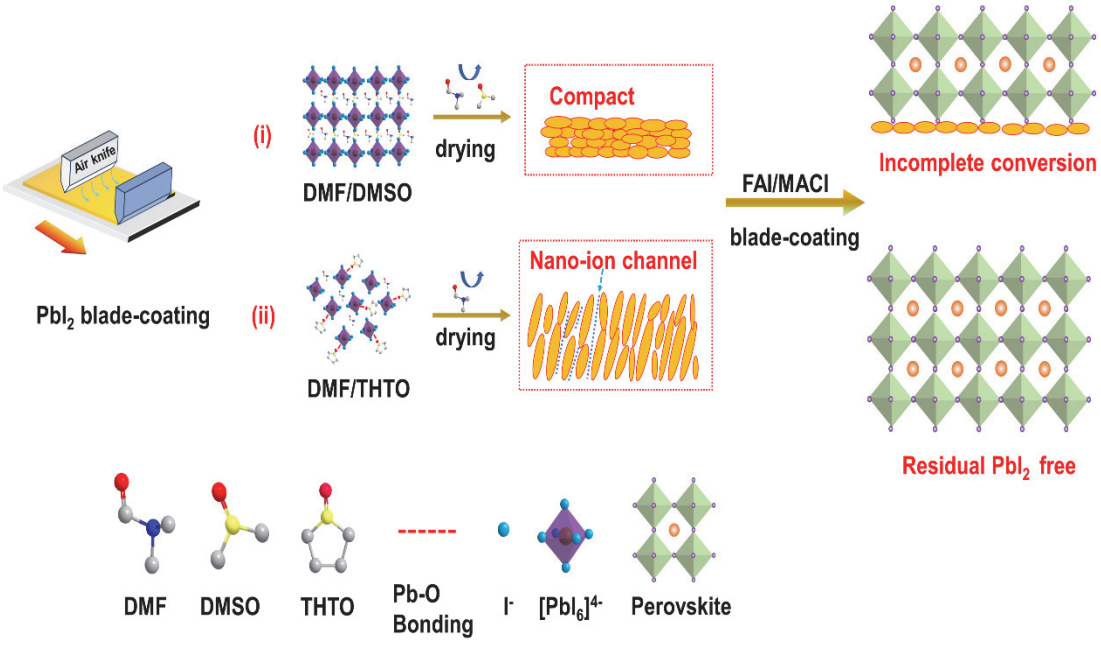

Fig. 1 Schematic diagram of the fabrication process of perovskite films *via* the blade-coating method from C-PbI_2 and THTO additive-induced NC-PbI_2 films.

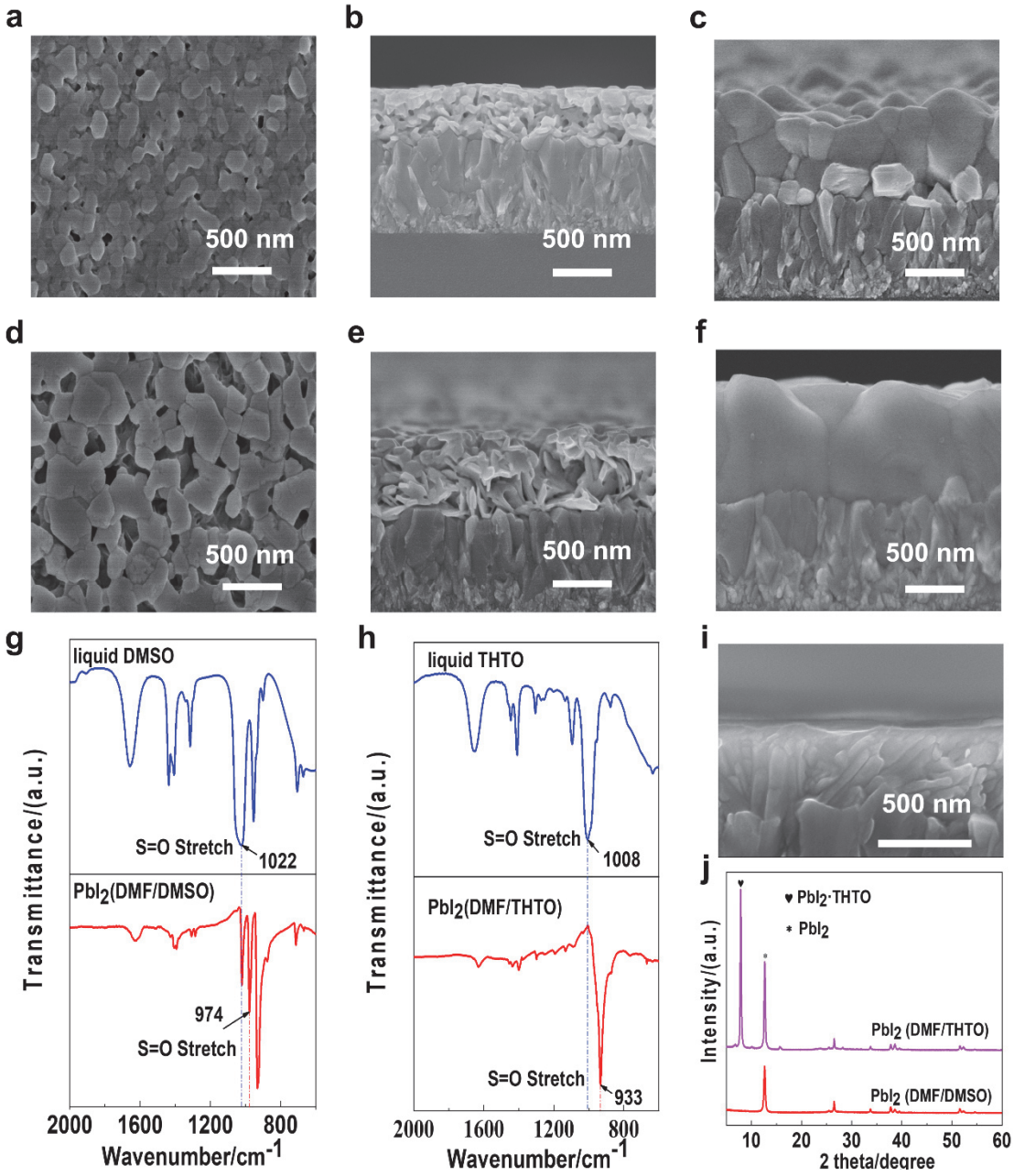

Fig. 2 The surface and cross-sectional SEM images of the blade-coated PbI_2 films: (a, b) C-PbI_2 and (d, e) NC-PbI_2. The cross-sectional SEM images of the blade-coated perovskite films converted from different blade-coated of (c) C-PbI_2 and (f) NC-PbI_2 films. FTIR spectra of (g) liquid DMSO (blue), PbI_2 (DMF/DMSO) films (red) and (h) liquid THTO (blue), PbI_2 (DMF/THTO) (red). (i) The cross-sectional SEM images of the blade-coated PbI_2 (THTO) films. (j) XRD patterns of the C-PbI_2 and NC-PbI_2 films.

(DMF/THTO) films. It can be clearly observed that a peak at 7.8° and a PbI_2 phase peak at 12.7° appear on the PbI_2-DMF/THTO films. While the PbI_2-DMF/DMSO films only have a PbI_2 peak at 12.7°. Therefore, it can be PbI_2·THTO complex proved that the vertical nanochannel inside the NC-PbI_2 films are caused *via* the complex phase generated by the complexation of PbI_2 and THTO.

The most striking difference in the XRD patterns between C-PbI_2 and NC-PbI_2 can be explained by "bond unsaturation" [41]. For this family of similar molecules, such as DMSO and THTO, the lower the Mayer bond order (MBO) and the higher the bond unsaturation value, the stronger complexing ability. It is found that the bond unsaturation 0.52 of THTO is higher than the bond unsaturation 0.49 of DMSO shown Table S1. Therefore, THTO have strongly interacts with the Pb^{2+} ion forming PbI_2·THTO complex after drying. In addition, Fig. 2g, h show the FTIR spectra for liquid DMSO (blue), PbI_2-DMF/DMSO (red) films and liquid THTO (blue), PbI_2-DMF/THTO (red) films, respectively. The stretching vibration peak of S=O appears at ~1022 cm^{-1} for liquid DMSO, shifting to ~974 cm^{-1} for the PbI_2-DMF/DMSO films, and the peak of liquid THTO appears at ~1008 cm^{-1}, shifting to 933 cm^{-1} for the PbI_2-DMF/THTO films.

The more intense low-frequency shift (75 cm^{-1}) for the PbI_2-DMF/THTO film displays the formation of stronger coordination bond between PbI_2 and THTO than that of DMSO (48 cm^{-1}) [42]. These results effectively demonstrate the strong interaction between PbI_2 and THTO, which is the cause forming the PbI_2·THTO complex.

Fig. 3a,b shows the XRD pattern of the perovskite films with various annealing time converted from blade-coated C-PbI_2 and NC-PbI_2 films, respectively. It is found that the un-annealed perovskite films converted from C-PbI_2 have a PbI_2 peak at 12.7°, while the films converted from NC-PbI_2 have no PbI_2 peak. This strongly proves that the NC-PbI_2 films can promote the complete reaction between PbI_2 and FAI without residual PbI_2. In addition, the diffraction peaks of PbI_2 in the C-PbI_2 and NC-PbI_2-converted perovskite films are continuously strengthened with the annealing process. This is attributed to the introduction of MACl that results in the decomposition of MA components during annealing [43]. Therefore, for the fully annealed perovskite film, the PbI_2 in the C-PbI_2 conversion-based perovskite film is excessively residual, which contains unreacted PbI_2 and the PbI_2 generated by the decomposition of the MA-based perovskite during annealing. For the fully annealed perovskite film based on NC-PbI_2 conversion, however, the diffraction peak intensity of the (110) plane of perovskite is significantly stronger than that of PbI_2, implying higher perovskite crystallinity and moderate of PbI_2 residues (Fig. S3). Moderate PbI_2 residues can effectively passivate defects and enhance the photovoltaic performance of PSCs, while excess PbI_2 can degrade the device performance [44–46]. Therefore, the quality of perovskite films obtained based on NC-PbI_2 conversion will be significantly improved. The perovskite grains converted from the C-PbI_2 (Fig. 3c) is much smaller than that from the NC-PbI_2 films (Fig. 3d). The average grain sizes of perovskite converted from the C-PbI_2 and NC-PbI_2 films are ~300 nm (Fig. S4a) and ~700 nm (Fig. S4b), respectively. Although the NC-PbI_2 film has a rougher surface, the converted perovskite film becomes much smooth due to the sufficient reaction. The roughness of the perovskite films obtained from Fig. S1c,d for the C-PbI_2 and NC-PbI_2 are 70 and 54 nm, respectively. This confirms the importance of controlling the morphology of the PbI_2 films on the crystallization of perovskite.

To investigate the charge carrier dynamics, the steady-state photoluminescence (PL) spectra (Fig. 3e) clearly observe that the NC-PbI_2 based perovskite film sample exhibits higher fluorescence intensity, which indicates that the quality of the perovskite films is greatly improved. In addition, time-resolved photoluminescence (TRPL) measurements are employed to evaluate the recombination behavior of the photoexcited carriers

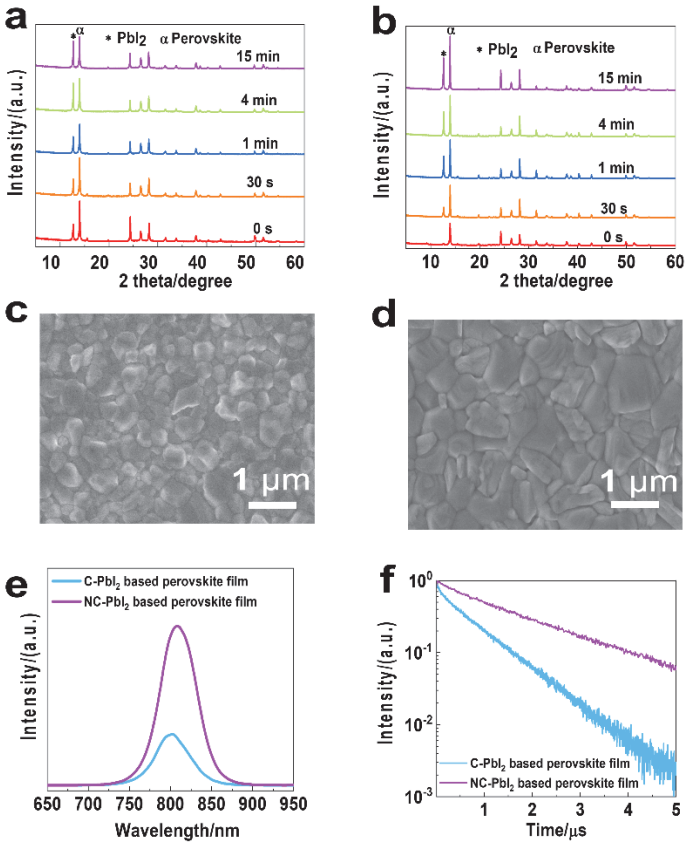

Fig. 3 The XRD patterns of the perovskite films with different annealing time converted from blade-coated of (a) C-PbI_2 and (b) NC-PbI_2 films. The surface SEM images of the perovskite films converted from (c) C-PbI_2 and (d) NC-PbI_2 films. (e) Steady-state PL spectra and (f) TRPL spectra of the blade-coated perovskite films converted from different PbI_2 films.

in the perovskite films (Fig. 3f). Correspondingly, the decay constants indicating the radiative recombination of free charge carriers that originate from the bulk perovskite obtained by a double exponential fitting increases from 0.80 to 1.86 μs for the perovskite films based on C-PbI_2 and NC-PbI_2. The reason for the prolonged life is that after the introduction of THTO, the nanochannel structure produced in the PbI_2 film significantly increases the grain size of the subsequently converted perovskite film, and reduces the concentration of surface and grain boundary defects.

To evaluate the effect of the bladed-coated different PbI_2 morphologies on the device performance, the converted perovskite films are made into compete devices with a structure of FTO/SnO_2/Perovskite/Spiro-OMeTAD/Au as shown in Fig. 4a. The current density-voltage (*J*–*V*) curves of the champion devices fabricated based on the C-PbI_2 and NC-PbI_2 are shown in Fig. S5a,b, respectively, and the corresponding photovoltaic characteristic distributions are shown in Figs. 4b and S6. The PCE in a reverse scan of the champion NC-PbI_2 device is 22.21% with an open-circuit photovoltage (V_{oc}) of 1.13 V, a short-circuit current density (J_{sc}) of 24.56 mA·cm^{-2}, and a fill factor (FF) of 0.80, which is the best reported PCE in literature based on the two-step sequential blade-coated perovskites as shown in Table S2. Compared with the C-PbI_2 device with the best PCE of 20.03% as shown in Fig. S5a, the photovoltaic performance has been greatly improved, indicating the essential of the improvement of PbI_2 morphology for the preparation of high-performance devices although it still has hysteresis.

To further eliminate the hysteresis, a large cation based iodide salt, tert-butylammonium iodide (*t*-BAI), was used to engineer the interface, which has been proved to be effective in suppressing hysteresis [47]. Fig. 4c shows the *J*–*V* curve of the champion device with the assisted interface treatment of *t*-BAI/IPA solution. Under the reverse scan, the PCE of the device is as high as 22.77% with a J_{sc} of 24.66 mA·cm^{-2}, a V_{oc} of 1.14 V, and an FF of 0.81, and the forward scanning efficiency is 21.30%. The external quantum efficiency (EQE) measurement (Fig. 4d) of the corresponding champion device was also performed to confirm the photocurrent, and the integrated current density is 24.38 mA·cm^{-2}, which matches well with the *J*–*V* results. Fig. 4e shows the steady-state power output of the champion device. Under a bias of 0.99 V, the steady-state output current density is 21.42 mA·cm^{-2}, and the corresponding efficiency is 21.21%.

Stability is also one of the essential properties of PSCs. Fig. S7 shows the storage stability of unencapsulated devices prepared with different PbI_2 morphologies at room temperature with a relative humidity of (20 ± 5)%. The NC-PbI_2 device retains more than 90% of the initial PCE of after being stored for 1000 h, showing excellent environmental stability, while the C-PbI_2 device only remains ~70% of the initial efficiency. In addition, the thermal stability of the devices without encapsulation under indoor conditions of 50 °C with a relative humidity of (20 ± 5)% was also tested. As shown in Fig. 4f, the NC-PbI_2 device exhibits an excellent thermal stability, retaining more than 80% of the initial PCE after more than 800 h under

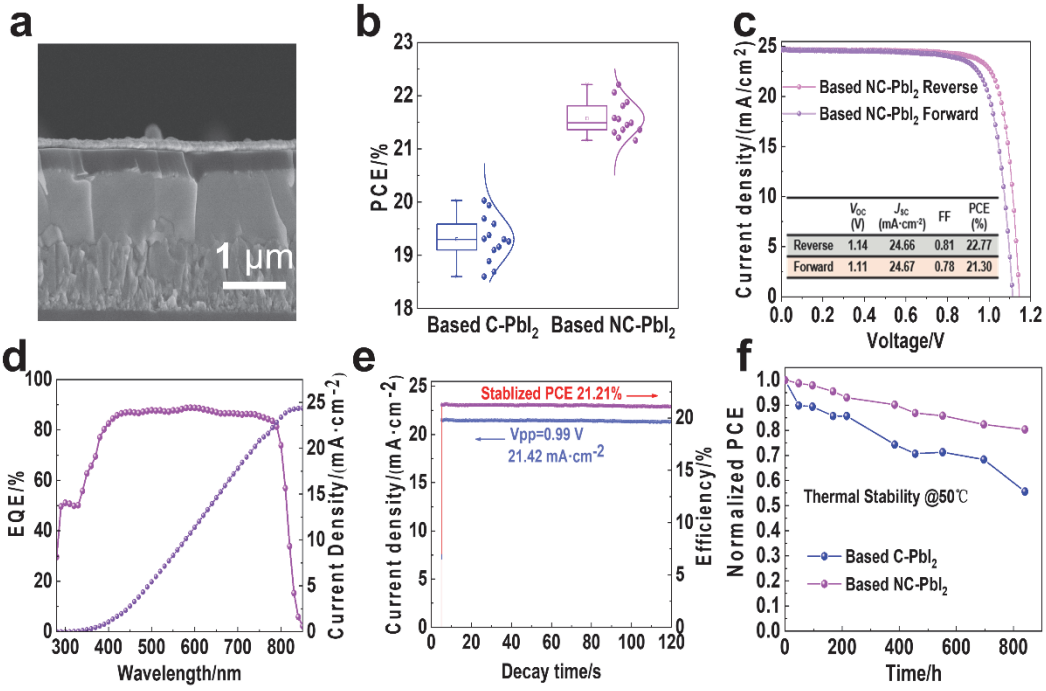

Fig. 4 (a) The cross-sectional SEM image of a PSC with the structure of FTO/SnO_2/Perovskite/Spiro-OMeTAD/Au. (b) PCE statistical distributions of PSCs prepared from different PbI_2 films. (c) Photovoltaic *J*–*V* curves, (d) EQE spectrum, and (e) the corresponding stable-state current output at the maximum power point of the champion NC-PbI_2 device treated with *t*-BAI. (f) Stability measurements of the non-encapsulated devices based on different PbI_2 morphologies at 50 °C in air with a relative humidity of (20 ± 5)%.

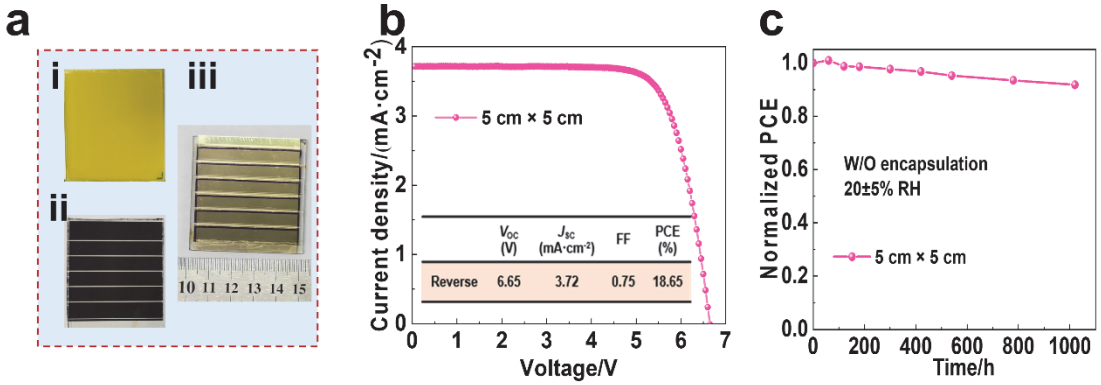

Fig. 5 (a) The photos of (i) NC-PbI_2 films, (ii) perovskite films, and (iii) perovskite solar module. (b) *J–V* curves of the optimal 25 cm^2 PSMs fabricated from the NC-PbI_2 films *via* the sequential bladed-coating process. (c) The stability measurements of 5 cm × 5 cm module performed in air at room temperature with a relative humidity of (20 ± 5)%.

ambient air conditions, whereas the C-PbI_2 device only remains about 50% of the initial PCE. The improved stability is due to the controlled microstructure of the PbI_2 film, which is beneficial to the complete conversion of high-quality perovskite.

Finally, to show the scalability, we successfully prepared a large-area perovskite film based on the NC-PbI_2 through two-step sequential blade-coating. The corresponding 5 cm × 5 cm PbI_2 film, perovskite film and perovskite solar module (PSM) photos are shown in Fig. 5a. The PSM based NC-PbI_2 with an active area of 10 cm^2 shows an outstanding photovoltaic performance (Fig. 5b), with a PCE of 18.65%, a J_{sc} of 3.72 mA·cm^{-2}, a V_{oc} of 6.65 V, and an FF of 0.75. However, the PSM based on the C-PbI_2 shows a relatively poor photovoltaic performance (Fig. S8), with a PCE of 15.23%, a J_{sc} of 3.70 mA·cm^{-2}, a V_{oc} of 6.31 V, and an FF of 0.65. This also further illustrates the control of the morphology of the PbI_2 film to prepare a high-performance perovskite solar module is an effective strategy. The PSM based NC-PbI_2 retains 90% of the original PCE after 1000 h storage without encapsulation as shown in Fig. 5c. As shown in Fig. S9, the NC-PbI_2 PSM exhibits an excellent thermal stability, retaining more than 70% of the initial PCE after more than 800 h under ambient air conditions. Therefore, through the strategy of controlling crystallization of PbI_2 to obtain optimized microstructure of the PbI_2 film, the application of two-step blade-coating to prepare the high-quality large-area perovskite film has shown great potential in the upscaling PSMs.

4 Conclusions

In summary, we have successfully prepared high-quality FA-based perovskite layers through the two-step sequential blade-coating method. By introducing the Lewis base THTO into the PbI_2 precursor solution to control the crystallization of PbI_2, vertical nanochannels are self-formed in the PbI_2 film. The PbI_2 film with vertical nanochannels provides continuous nanochannels for the penetration of FAI molecules and larger interface reaction area than the compact PbI_2 film. This method is conducive to the complete conversion of PbI_2 into perovskite, and the grain size and crystallinity of the perovskite film are greatly improved. A FA-based device with the highest PCE of 22.77% is achieved *via* this sequential blade-coating strategy. Large PSMs with the area of 5 cm × 5 cm were also prepared, achieving an efficiency of 18.65%. In addition, unencapsulated small-area devices and large-area modules show excellent stability in ambient air. This two-step sequential blade-coating method has successfully demonstrated in fabrication of large-area high-quality FA-based perovskite films, showing a broad application prospect for the scaling up PSCs.

Acknowledgements: The Analytical and Testing Centre of Wuhan University of Technology and Hubei Key Laboratory of Low Dimensional Optoelectronic Material and Devices, Hubei University of Arts and Science are acknowledged for the XRD and SEM characterizations.

References

(1) Yin, W. J.; Shi, T.; Yan, Y. *Adv. Mater.* **2014,** *26*, 4653. doi: 10.1002/adma.201306281

(2) Cheng, Y. B.; Pascoe, A.; Huang, F. Z.; Peng, Y. *Nature* **2016,** *539*, 488. doi: 10.1038/539488a

(3) Saliba, M.; Matsui, T.; Domanski, K.; Seo, J. Y.; Ummadisingu, A.; Zakeeruddin, S. M.; Correa-Baena, J. P.; Tress, W. R.; Abate, A.; Hagfeldt, A.; *et al. Science* **2016,** *354*, 206. doi: 10.1126/science.aah5557

(4) Bu, T. L.; Li, J.; Li, H.Y.; Tian, C. C.; Su, J.; Tong, G.; Ono Luis, K.; Wang, C.; Lin, Z. P.; Chai, N. Y.; *et al. Science* **2021,** *372*, 1327. doi: 10.1126/science.abh1035

(5) Mo, Y. P.; Wang, C.; Zheng, X. T.; Zhou, P.; Li, J.; Yu, X. X.; Yang, K. Z.; Deng, X.Y.; Park, H.; Huang, F. Z.; *et al. Interdiscip. Mater.* **2022,** (in press). doi: 10.1002/idm2.12022

(6) Yin, Y., Guo Z. D., Chen, G. Y, Zhang, H. F., Yin, W. J. *Acta Phys. -Chim Sin.* **2021,** *37*, 2008048. [尹媛, 郭振东, 陈高远, 张慧峰, 尹万健. 物理化学学报, **2021,** *37*, 2008048.]

doi: 10.3866/PKU.WHXB202008048

(7) Ji, J, Liu, X., Huang, H., Jiang, H. R., Duan, M. J., Liu, B. Y., Cui, P., Li, Y. F., Li, M. C. *Acta Phys. -Chim Sin.* **2021,** *37*, 2008095. [纪军, 刘新, 黄浩, 蒋皓然, 段明君, 刘本玉, 崔鹏, 李英峰, 李美成. 物理化学学报, **2021,** *37*, 2008095.] doi: 10.3866/PKU.WHXB202008095

(8) Min, H.; Lee, D. Y.; Kim, J.; Kim, G.; Lee, K. S.; Kim, J.; Paik, M. J.; Kim, Y. K.; Kim, K. S.; Kim, M. G.; *et al. Nature* **2021,** *598*, 444. doi: 10.1038/s41586-021-03964-8

(9) Kanda, H.; Dan Mihailetchi, V.; Gueunier-Farret, M.-E.; Kleider, J.-P.; Djebbour, Z.; Alvarez, J.; Philippe, B.; Isabella, O.; Vogt, M. R.; Santbergen, R.; *et al. Interdiscip. Mater.* **2022,** *1*, 148. doi: 10.1002/idm2.12006

(10) Huang, F. Z.; Dkhissi, Y.; Huang, W. C.; Xiao, M. D.; Benesperi, I.; Rubanov, S.; Zhu, Y.; Lin, X. F.; Jiang, L. C.; Zhou, Y. C.; *et al. Nano Energy* **2014,** *10*, 10. doi: 10.1016/j.nanoen.2014.08.015

(11) Zhang, M.; Yun, J. S.; Ma, Q. S.; Zheng, J. H.; Lau, C. F. J.; Deng, X. F.; Kim, J.; Kim, D.; Seidel, J.; Green, M. A.; *et al. ACS Energy Lett.* **2017,** *2*, 438. doi: 10.1021/acsenergylett.6b00697

(12) Dualeh, A.; Tétreault, N.; Moehl, T.; Gao, P.; Nazeeruddin, M. K.; Grätzel, M. *Adv. Funct. Mater.* **2014,** *24*, 3250. doi: 10.1002/adfm.201304022

(13) Rong, Y.; Hu, Y.; Mei, A.; Tan, H.; Saidaminov, M. I.; Seok, S. I.; McGehee, M. D.; Sargent, E. H.; Han, H. *Science* **2018,** *361*, eaat8235. doi: 10.1126/science.aat8235

(14) Swartwout, R.; Hoerantner, M. T.; Bulović, V. *Energy Environ. Mater.* **2019,** *2*, 119. doi: 10.1002/eem2.12043

(15) Rong, Y.; Ming, Y.; Ji, W.; Li, D.; Mei, A.; Hu, Y.; Han, H. *J. Phys. Chem. Lett.* **2018,** *9*, 2707. doi: 10.1021/acs.jpclett.8b00912

(16) Xiao, Y.; Zuo, C.; Zhong, J. X.; Wu, W. Q.; Shen, L.; Ding, L. *Adv. Energy Mater.* **2021,** *11*, 2100378. doi: 10.1002/aenm.202100378

(17) Zhang, L.; Lin, B.; Hu, B.; Xu, X.; Ma, W. *Adv. Mater.* **2018,** *30*, e1800343. doi: 10.1002/adma.201800343

(18) Guo, F.; He, W.; Qiu, S.; Wang, C.; Liu, X.; Forberich, K.; Brabec, C. J.; Mai, Y. *Adv. Funct. Mater.* **2019,** *29*, 1900964. doi: 10.1002/adfm.201900964

(19) He, M.; Li, B.; Cui, X.; Jiang, B.; He, Y.; Chen, Y.; O'Neil, D.; Szymanski, P.; Ei-Sayed, M. A.; Huang, J.; *et al. Nat. Commun.* **2017,** *8*, 16045. doi: 10.1038/ncomms16045

(20) Hu, H. L.; Ren, Z. W.; Fong, P. W. K.; Qin, M. C.; Liu, D. J.; Lei, D. Y.; Lu, X. H.; Li, G. *Adv. Funct. Mater.* **2019,** *29*, 1900092. doi: 10.1002/adfm.201900092

(21) Jeong, D.-N.; Lee, D.-K.; Seo, S.; Lim, S. Y.; Zhang, Y.; Shin, H.; Cheong, H.; Park, N.-G. *ACS Energy Lett.* **2019,** *4*, 1189. doi: 10.1021/acsenergylett.9b00042

(22) Yang, M.; Li, Z.; Reese, M. O.; Reid, O. G.; Kim, D. H.; Siol, S.; Klein, T. R.; Yan, Y.; Berry, J. J.; van Hest, M. F. A. M.; *et al. Nat. Energy* **2017,** *2*, 17038. doi: 10.1038/nenergy.2017.38

(23) Zheng, X.; Deng, Y.; Chen, B.; Wei, H.; Xiao, X.; Fang, Y.; Lin, Y.; Yu, Z.; Liu, Y.; Wang, Q.; *et al. Adv. Mater.* **2018,** *30*, e1803428. doi: 10.1002/adma.201803428

(24) Deng, Y. H.; Zheng, X. P.; Bai, Y.; Wang, Q.; Zhao, J. J.; Huang, J. S. *Nat. Energy* **2018,** *3*, 560. doi: 10.1038/s41560-018-0153-9

(25) Tait, J. G.; Merckx, T.; Li, W.; Wong, C.; Gehlhaar, R.; Cheyns, D.; Turbiez, M.; Heremans, P. *Adv. Funct. Mater.* **2015,** *25*, 3393. doi: 10.1002/adfm.201501039

(26) Deng, Y. H.; Peng, E.; Shao, Y. C.; Xiao, Z. G.; Dong, Q. F.; Huang, J. S. *Energy Environ. Sci.* **2015,** *8*, 1544. doi: 10.1039/c4ee03907f

(27) Deng, Y. H.; Van Brackle, C. H.; Dai, X. Z.; Zhao, J. J.; Chen, B.; Huang, J. S. *Sci. Adv.* **2019,** *5*, eaax7537. doi: 10.1126/sciadv.aax7537

(28) Lu, Y., Ge Y., Sui, M. L. *Acta Phys. -Chim. Sin.* **2022,** *38*, 2007088. [卢岳, 葛杨, 隋曼龄. 物理化学学报, **2022,** *38*, 2007088.] doi: 10.3866/PKU.WHXB202007088

(29) Min, H.; Kim, M.; Lee, S.-U.; Kim, H.; Kim, G.; Choi, K.; Lee Jun, H.; Seok Sang, I. *Science* **2019,** *366*, 749. doi: 10.1126/science.aay7044

(30) Kim, M.; Kim, G.-H.; Lee, T. K.; Choi, I. W.; Choi, H. W.; Jo, Y.; Yoon, Y. J.; Kim, J. W.; Lee, J.; Huh, D.; *et al. Joule* **2019,** *3*, 2179. doi: 10.1016/j.joule.2019.06.014

(31) Wang, M. H.; Tan, S. U.; Zhao, Y. P.; Zhu, P. C.; Yin, Y. F.; Feng, Y. L.; Huang, T. Y.; Xue, J. J.; Wang, R.; Han, G. S.; *et al. Adv. Funct. Mater.* **2020,** *31*, 2007520. doi: 10.1002/adfm.202007520

(32) Nan, Z. A.; Chen, L.; Liu, Q.; Wang, S. H.; Chen, Z. X.; Kang, S. Y.; Ji, J. B.; Tan, Y. Y.; Hui, Y.; Yan, J. W.; *et al. Chem* **2021,** *7*, 2513. doi: 10.1016/j.chempr.2021.07.011

(33) Doherty, T. A. S.; Nagane, S.; Kubicki, D. J.; Jung, Y.-K.; Johnstone, D. N.; Iqbal, A. N.; Guo, D. Y.; Frohna, K.; Danaie, M.; Tennyson, E. M.; *et al. Science* **2021,** *374*, 1598. doi: 10.1126/science.abl4890

(34) Yang, F.; Dong, L. R.; Jang, D. J.; Tam, K. C.; Zhang, K. C.; Li, N.; Guo, F.; Li, C.; Arrive, C.; Bertrand, M.; *et al. Adv. Energy Mater.* **2020,** *10*, 2001869. doi: 10.1002/aenm.202001869

(35) Li, Z.; Klein, T. R.; Kim, D. H.; Yang, M. J.; Berry, J. J.; van Hest, M. F. A. M.; Zhu, K. *Nat. Rev. Mater.* **2018,** *3*, 18017. doi: 10.1038/natrevmats.2018.17

(36) Chen, H. N. *Adv. Funct. Mater.* **2017,** *27*, 1605654. doi: 10.1002/adfm.201605654

(37) Zhang, W. H.; Xiong, J.; Jiang, L.; Wang, J. Y.; Mei, T.; Wang, X. B.; Gu, H. S.; Daoud, W. A.; Li, J. H. *ACS Appl. Mater. Interfaces* **2017,** *9*, 38467. doi: 10.1021/acsami.7b10994

(38) Zhang, H.; Mao, J.; He, H. X.; Zhang, D.; Zhu, H. L.; Xie, F. X.; Wong, K. S.; Gratzel, M.; Choy, W. C. H. *Adv. Energy Mater.* **2015,** *5*, 1501354. doi: 10.1002/aenm.201501354

(39) Hui, W.; Chao, L. F.; Lu, H.; Xia, F.; Wei, Q.; Su, Z. H.; Niu, T. T.;

Tao, L.; Du, B.; Li, D.; *et al. Science* **2021,** *371*, 1359. doi: 10.1126/science.abf7652

(40) Zhang, J. W.; Bu, T. L.; Li, J.; Li, H. Y.; Mo, Y. P.; Wu, Z. L.; Liu, Y. F.; Zhang, X. L.; Cheng, Y. B.; Huang, F. Z. *J. Mater. Chem. A* **2020,** *8*, 8447. doi: 10.1039/d0ta02043e

(41) Foley, B. J.; Girard, J.; Sorenson, B. A.; Chen, A. Z.; Scott Niezgoda, J.; Alpert, M. R.; Harper, A. F.; Smilgies, D.-M.; Clancy, P.; Saidi, W. A.; *et al. J. Mater. Chem. A* **2017,** *5*, 113. doi: 10.1039/c6ta07671h

(42) Wang, S. B.; Chen, Y. Q.; Li, R. Y.; Xu, Y. B.; Feng, J. S.; Yang, D.; Yuan, N. Y.; Zhang, W. H.; Liu, S. F.; Ding, J. N. *Adv. Sci.* **2020,** *7*, 1903009. doi: 10.1002/advs.201903009

(43) Ye, F. H.; Ma, J. J.; Chen, C.; Wang, H. B.; Xu, Y. H.; Zhang, S. P.; Wang, T.; Tao, C.; Fang, G. J. *Adv. Mater.* **2021,** *33*, e2007126. doi: 10.1002/adma.202007126

(44) Jiang, Q.; Chu, Z.; Wang, P. Y.; Yang, X.; Liu, H.; Wang, Y.; Yin, Z. G.; Wu, J. L.; Zhang, X. W.; You, J. B. *Adv. Mater.* **2017,** *29*, 1703852. doi: 10.1002/adma.201703852

(45) Tumen-Ulzii, G.; Qin, C.; Klotz, D.; Leyden, M. R.; Wang, P.; Auffray, M.; Fujihara, T.; Matsushima, T.; Lee, J.-W.; Lee, S.-J.; *et al. Adv. Mater.* **2020,** *32*, 1905035. doi: 10.1002/adma.201905035

(46) Liu, F. Z.; Dong, Q.; Wong, M. K.; Djurišić, A. B.; Ng, A.; Ren, Z. W.; Shen, Q.; Surya, C.; Chan, W. K.; Wang, J.; *et al. Adv. Energy Mater.* **2016,** *6*, 1502206. doi: 10.1002/aenm.201502206

(47) Bu, T. L.; Li, J.; Huang, W. C.; Mao, W. X.; Zheng, F.; Bi, P. Q.; Hao, X. T.; Zhong, J.; Cheng, Y. B.; Huang, F. Z. *J. Mater. Chem. A* **2019,** *7*, 6793. doi: 10.1039/c8ta12284a